

Using optical trap to measure the refractive index of a single animal virus in culture fluid with high precision

Yuanjie Pang,¹ Hanna Song,¹ and Wei Cheng^{1,2,3,*}

¹Department of Pharmaceutical Sciences, College of Pharmacy, University of Michigan, 428 Church Street, Ann Arbor, Michigan 48109, USA

²Department of Biological Chemistry, University of Michigan Medical School, Ann Arbor, Michigan 48109, USA

³Department of Biophysics, University of Michigan, Ann Arbor, Michigan 48109, USA

*chengwe@umich.edu

Abstract: The refractive index (RI) is a fundamental parameter of materials that can be used to distinguish and sort materials of different nature. Although the RI of a virus is required for many optics-based biosensing applications, RIs of animal viruses have never been measured. Here we have developed a technique that can measure the RI of individual viruses in aqueous media with high precision. This technique is based on optical trapping of single virions and works by relating the size and RI of a single virus to the stiffness of an optical trap. We have derived an analytic expression to quantitatively describe the optical trapping of these particles. We have validated this equation using nanoparticles of known RI, and measured the RI of individual human immunodeficiency viruses type-1, which yielded a value of 1.42 at 830 nm with less than 2% coefficient of variation. This value is much lower than the RI typically assumed for viruses, but very close to that of 2.0 M sucrose solution in water. To the best of our knowledge, this is the first report on the experimental measurement of the RI for a single animal virus in aqueous media. This technique does not require prior knowledge on the diameter of the nanoparticles, and can be applied to other viruses or nanoparticles for accurate measurement of RI that is critical for the label-free detection of these particles in various settings.

© 2016 Optical Society of America

OCIS codes: (140.7010) Laser trapping; (350.4855) Optical tweezers or optical manipulation; (170.4520) Optical confinement and manipulation; (160.1435) Biomaterials; (350.4990) Particles.

References and links

1. M. P. MacDonald, G. C. Spalding, and K. Dholakia, "Microfluidic sorting in an optical lattice," *Nature* **426**(6965), 421–424 (2003).
2. Y. Zhang, H. X. Lei, and B. J. Li, "Refractive-Index-Based Sorting of Colloidal Particles Using a Subwavelength Optical Fiber in a Static Fluid," *Appl. Phys. Express* **6**(7), 072001 (2013).
3. E. van der Pol, F. A. W. Coumans, A. Sturk, R. Nieuwland, and T. G. van Leeuwen, "Refractive Index Determination of Nanoparticles in Suspension Using Nanoparticle Tracking Analysis," *Nano Lett.* **14**(11), 6195–6201 (2014).
4. G. Knöner, S. Parkin, T. A. Nieminen, N. R. Heckenberg, and H. Rubinsztein-Dunlop, "Measurement of the index of refraction of single microparticles," *Phys. Rev. Lett.* **97**(15), 157402 (2006).
5. J. Beuthan, O. Minet, J. Helfmann, M. Herrig, and G. Müller, "The spatial variation of the refractive index in biological cells," *Phys. Med. Biol.* **41**(3), 369–382 (1996).
6. F. P. Bolin, L. E. Preuss, R. C. Taylor, and R. J. Ference, "Refractive Index of Some Mammalian Tissues Using A Fiber Optic Cladding Method," *Appl. Opt.* **28**(12), 2297–2303 (1989).
7. H. Li and S. Xie, "Measurement method of the refractive index of biotissue by total internal reflection," *Appl. Opt.* **35**(10), 1793–1795 (1996).
8. H. Ewers, V. Jacobsen, E. Klotzsch, A. E. Smith, A. Helenius, and V. Sandoghdar, "Label-free optical detection

- and tracking of single virions bound to their receptors in supported membrane bilayers,” *Nano Lett.* **7**(8), 2263–2266 (2007).
9. G. G. Daaboul, A. Yurt, X. Zhang, G. M. Hwang, B. B. Goldberg, and M. S. Ünlü, “High-Throughput Detection and Sizing of Individual Low-Index Nanoparticles and Viruses for Pathogen Identification,” *Nano Lett.* **10**(11), 4727–4731 (2010).
 10. S. Liu, Y. Zhao, J. W. Parks, D. W. Deamer, A. R. Hawkins, and H. Schmidt, “Correlated Electrical and Optical Analysis of Single Nanoparticles and Biomolecules on a Nanopore-Gated Optofluidic Chip,” *Nano Lett.* **14**(8), 4816–4820 (2014).
 11. F. Shen, J. Wang, Z. Xu, Y. Wu, Q. Chen, X. Li, X. Jie, L. Li, M. Yao, X. Guo, and T. Zhu, “Rapid Flu Diagnosis Using Silicon Nanowire Sensor,” *Nano Lett.* **12**(7), 3722–3730 (2012).
 12. J. A. Arter, D. K. Taggart, J. E. Diaz, R. M. Penner, and G. A. Weiss, “Virus-PEDOT nanowires for biosensing,” *Abstracts of Papers of the American Chemical Society* **241**, 1 (2011).
 13. S. Shanmukh, L. Jones, J. Driskell, Y. Zhao, R. Dluhy, and R. A. Tripp, “Rapid and sensitive detection of respiratory virus molecular signatures using a silver nanorod array SERS substrate,” *Nano Lett.* **6**(11), 2630–2636 (2006).
 14. X. Fan, I. M. White, S. I. Shopova, H. Zhu, J. D. Suter, and Y. Sun, “Sensitive optical biosensors for unlabeled targets: a review,” *Anal. Chim. Acta* **620**(1-2), 8–26 (2008).
 15. P. Kang, P. Schein, X. Serey, D. O’Dell, and D. Erickson, “Nanophotonic detection of freely interacting molecules on a single influenza virus,” *Sci. Rep.* **5**, 12087 (2015).
 16. M. C. DeSantis and W. Cheng, “Label-free detection and manipulation of single biological nanoparticles,” *Wiley Interdiscip. Rev. Nanomed. Nanobiotechnol.* in press (2016).
 17. H. Zhu, I. M. White, J. D. Suter, M. Zourob, and X. Fan, “Opto-fluidic micro-ring resonator for sensitive label-free viral detection,” *Analyst (Lond.)* **133**(3), 356–360 (2008).
 18. F. Vollmer, S. Arnold, and D. Keng, “Single virus detection from the reactive shift of a whispering-gallery mode,” *Proc. Natl. Acad. Sci. U.S.A.* **105**(52), 20701–20704 (2008).
 19. T. Lu, H. Lee, T. Chen, S. Herchak, J. H. Kim, S. E. Fraser, R. C. Flagan, and K. Vahala, “High sensitivity nanoparticle detection using optical microcavities,” *Proc. Natl. Acad. Sci. U.S.A.* **108**(15), 5976–5979 (2011).
 20. A. Mitra, B. Deutsch, F. Ignatovich, C. Dykes, and L. Novotny, “Nano-optofluidic Detection of Single Viruses and Nanoparticles,” *ACS Nano* **4**(3), 1305–1312 (2010).
 21. O. Block, A. Mitra, L. Novotny, and C. Dykes, “A rapid label-free method for quantitation of human immunodeficiency virus type-1 particles by nanospectroscopy,” *J. Virol. Methods* **182**(1-2), 70–75 (2012).
 22. A. Ymeti, J. S. Kanger, J. Greve, P. V. Lambeck, R. Wijn, and R. G. Heideman, “Realization of a multichannel integrated Young interferometer chemical sensor,” *Appl. Opt.* **42**(28), 5649–5660 (2003).
 23. A. Ymeti, J. S. Kanger, J. Greve, G. A. J. Besselink, P. V. Lambeck, R. Wijn, and R. G. Heideman, “Integration of microfluidics with a four-channel integrated optical Young interferometer immunosensor,” *Biosens. Bioelectron.* **20**(7), 1417–1421 (2005).
 24. A. Ymeti, J. Greve, P. V. Lambeck, T. Wink, S. W. van Hövell, T. A. M. Beumer, R. R. Wijn, R. G. Heideman, V. Subramaniam, and J. S. Kanger, “Fast, ultrasensitive virus detection using a young interferometer sensor,” *Nano Lett.* **7**(2), 394–397 (2007).
 25. J. Xu, D. Suarez, and D. S. Gottfried, “Detection of avian influenza virus using an interferometric biosensor,” *Anal. Bioanal. Chem.* **389**(4), 1193–1199 (2007).
 26. B. M. McDermott, Jr., A. H. Rux, R. J. Eisenberg, G. H. Cohen, and V. R. Racaniello, “Two distinct binding affinities of poliovirus for its cellular receptor,” *J. Biol. Chem.* **275**(30), 23089–23096 (2000).
 27. A. A. Yanik, M. Huang, O. Kamohara, A. Artar, T. W. Geisbert, J. H. Connor, and H. Altug, “An Optofluidic Nanoplasmonic Biosensor for Direct Detection of Live Viruses from Biological Media,” *Nano Lett.* **10**(12), 4962–4969 (2010).
 28. S. Wang, X. Shan, U. Patel, X. Huang, J. Lu, J. Li, and N. Tao, “Label-free imaging, detection, and mass measurement of single viruses by surface plasmon resonance,” *Proc. Natl. Acad. Sci. U.S.A.* **107**(37), 16028–16032 (2010).
 29. J. H. Kim, H. Song, J. L. Austin, and W. Cheng, “Optimized Infectivity of the Cell-Free Single-Cycle Human Immunodeficiency Viruses Type 1 (HIV-1) and Its Restriction by Host Cells,” *PLoS One* **8**(6), e67170 (2013).
 30. J. W. Bess, Jr., R. J. Gorelick, W. J. Bosche, L. E. Henderson, and L. O. Arthur, “Microvesicles are a source of contaminating cellular proteins found in purified HIV-1 preparations,” *Virology* **230**(1), 134–144 (1997).
 31. P. Gluschkof, I. Mondor, H. R. Gelderblom, and Q. J. Sattentau, “Cell membrane vesicles are a major contaminant of gradient-enriched human immunodeficiency virus type-1 preparations,” *Virology* **230**(1), 125–133 (1997).
 32. T. Tlusty, A. Meller, and R. Bar-Ziv, “Optical gradient forces of strongly localized fields,” *Phys. Rev. Lett.* **81**(8), 1738–1741 (1998).
 33. Y. Pang, H. Song, J. H. Kim, X. Hou, and W. Cheng, “Optical trapping of individual human immunodeficiency viruses in culture fluid reveals heterogeneity with single-molecule resolution,” *Nat. Nanotechnol.* **9**(8), 624–630 (2014).
 34. S. F. Tolic-Norrelykke, E. Schaffer, J. Howard, F. S. Pavone, F. Julicher, and H. Flyvbjerg, “Calibration of optical tweezers with positional detection in the back focal plane,” *Rev. Sci. Instrum.* **77**(10), 103101 (2006).
 35. J. H. Kim, H. Song, J. L. Austin, and W. Cheng, “Optimized Infectivity of the Cell-Free Single-Cycle Human Immunodeficiency Viruses Type 1 (HIV-1) and Its Restriction by Host Cells,” *PLoS One* **8**(6), e67170 (2013).

36. P. M. Bendix and L. B. Oddershede, "Expanding the Optical Trapping Range of Lipid Vesicles to the Nanoscale," *Nano Lett.* **11**(12), 5431–5437 (2011).
37. W. Cheng, X. Hou, and F. Ye, "Use of tapered amplifier diode laser for biological-friendly high-resolution optical trapping," *Opt. Lett.* **35**(17), 2988–2990 (2010).
38. F. Gittes and C. F. Schmidt, "Interference model for back-focal-plane displacement detection in optical tweezers," *Opt. Lett.* **23**(1), 7–9 (1998).
39. W. Cheng, S. G. Arunajadai, J. R. Moffitt, I. Tinoco, Jr., and C. Bustamante, "Single-Base Pair Unwinding and Asynchronous RNA Release by the Hepatitis C Virus NS3 Helicase," *Science* **333**(6050), 1746–1749 (2011).
40. M. C. Wang and G. E. Uhlenbeck, "On the Theory of the Brownian Motion-II," *Rev. Mod. Phys.* **17**(2-3), 323–342 (1945).
41. A. B. Stilgoe, T. A. Nieminen, G. Knöener, N. R. Heckenberg, and H. Rubinsztein-Dunlop, "The effect of Mie resonances on trapping in optical tweezers," *Opt. Express* **16**(19), 15039–15051 (2008).
42. J. J. Xiao, J. Ng, Z. F. Lin, and C. T. Chan, "Whispering gallery mode enhanced optical force with resonant tunneling excitation in the Kretschmann geometry," *Appl. Phys. Lett.* **94**(1), 011102 (2009).
43. A. Ashkin, J. M. Dziedzic, J. E. Bjorkholm, and S. Chu, "Observation of a Single-Beam Gradient Force Optical Trap for Dielectric Particles," *Opt. Lett.* **11**(5), 288–290 (1986).
44. Y. Harada and T. Asakura, "Radiation forces on a dielectric sphere in the Rayleigh scattering regime," *Opt. Commun.* **124**(5-6), 529–541 (1996).
45. J. D. Jackson, *Classical Electrodynamics*, 3rd ed. (Wiley-VCH, 1998), Chap. 10.
46. A. Ashkin, "Forces of a single-beam gradient laser trap on a dielectric sphere in the ray optics regime," *Biophys. J.* **61**(2), 569–582 (1992).
47. B. Richards and E. Wolf, "Electromagnetic diffraction in optical systems. 2. structure of the image field in an aplanatic system," *Proceedings of the Royal Society of London Series a-Mathematical and Physical Sciences* **253**, 358–379 (1959).
48. M. C. Teich and B. Saleh, "Fundamentals of photonics," Canada, Wiley Interscience, 3 (1991).
49. N. Sultanova, S. Kasarova, and I. Nikolov, "Dispersion Properties of Optical Polymers," *Acta Phys. Pol. A* **116**(4), 585–587 (2009).
50. M. Bass, C. DeCusatis, J. Enoch, V. Lakshminarayanan, G. Li, C. MacDonald, V. Mahajan, and E. Van Stryland, "Handbook of Optics, Volume IV: Optical Properties of Materials," *Nonlinear Optics, Quantum Optics* **4**(2009).
51. J. A. G. Briggs, T. Wilk, R. Welker, H. G. Kräusslich, and S. D. Fuller, "Structural organization of authentic, mature HIV-1 virions and cores," *EMBO J.* **22**(7), 1707–1715 (2003).
52. P. Zhu, J. Liu, J. Bess, Jr., E. Chertova, J. D. Lifson, H. Grisé, G. A. Ofek, K. A. Taylor, and K. H. Roux, "Distribution and three-dimensional structure of AIDS virus envelope spikes," *Nature* **441**(7095), 847–852 (2006).
53. P. R. Cooper, "Refractive-Index Measurements of Liquids Used in Conjunction with Optical Fibers," *Appl. Opt.* **22**(19), 3070–3072 (1983).
54. J. Rheims, J. Koser, and T. Wriedt, "Refractive-index measurements in the near-IR using an Abbe refractometer," *Meas. Sci. Technol.* **8**(6), 601–605 (1997).
55. S. Kedenburg, M. Vieweg, T. Gissibl, and H. Giessen, "Linear refractive index and absorption measurements of nonlinear optical liquids in the visible and near-infrared spectral region," *Opt. Mater. Express* **2**(11), 1588–1611 (2012).
56. W. M. Balch, J. Vaughn, J. Navotny, D. T. Drapeau, R. Vaillancourt, J. Lapierre, and A. Ashe, "Light scattering by viral suspensions," *Limnol. Oceanogr.* **45**(2), 492–498 (2000).
57. M. A. Taubenblatt and J. S. Batchelder, "Measurement of the size and refractive index of a small particle using the complex forward-scattered electromagnetic field," *Appl. Opt.* **30**(33), 4972–4979 (1991).
58. P. Stoller, V. Jacobsen, and V. Sandoghdar, "Measurement of the complex dielectric constant of a single gold nanoparticle," *Opt. Lett.* **31**(16), 2474–2476 (2006).
59. C. M. Trubey, E. Chertova, L. V. Coren, J. M. Hilburn, C. V. Hixson, K. Nagashima, J. D. Lifson, and D. E. Ott, "Quantitation of HLA class II protein incorporated into human immunodeficiency type 1 virions purified by anti-CD45 immunofluorescence depletion of microvesicles," *J. Virol.* **77**(23), 12699–12709 (2003).
60. D. McDonald, M. A. Vodicka, G. Lucero, T. M. Svitkina, G. G. Borisy, M. Emerman, and T. J. Hope, "Visualization of the intracellular behavior of HIV in living cells," *J. Cell Biol.* **159**(3), 441–452 (2002).
61. L. A. Carlson, J. A. Briggs, B. Glass, J. D. Riches, M. N. Simon, M. C. Johnson, B. Müller, K. Grunewald, and H. G. Kräusslich, "Three-dimensional analysis of budding sites and released virus suggests a revised model for HIV-1 morphogenesis," *Cell Host Microbe* **4**(6), 592–599 (2008).
62. L. A. Carlson, J. A. G. Briggs, B. Glass, J. D. Riches, M. N. Simon, M. C. Johnson, B. Müller, K. Grunewald, and H. G. Kräusslich, "Three-Dimensional Analysis of Budding Sites and Released Virus Suggests a Revised Model For HIV-1 Morphogenesis," *Cell Host Microbe* **4**(6), 592–599 (2008).
63. D. Knipe, P. Howley, D. Griffin, R. Lamb, M. Martin, B. Roizman, and S. Straus, *Fields Virology* (Lippincott Williams & Wilkins, 2007).
64. T. A. Nieminen, V. L. Y. Loke, A. B. Stilgoe, G. Knöner, A. M. Branczyk, N. R. Heckenberg, and H. Rubinsztein-Dunlop, "Optical tweezers computational toolbox," *J. Opt. A, Pure Appl. Opt.* **9**(8), S196–S203 (2007).

1. Introduction

The refractive index (RI), defined as the ratio between the speeds of light in vacuum relative to that in the material of interest, is a fundamental parameter of materials. Because RI is related to the composition of materials, it potentially offers a label-free parameter for distinction and sorting of materials of different nature [1–3]. The RI of homogeneous materials that are readily available in microliter to milliliter quantities can be measured using refractometers. Alternatively, the RI of single microparticles of different materials can be measured based on a numerical T-matrix approach using optical tweezers [4]. In contrast, biological materials are known to display heterogeneity in RI [5]. As a result, it is difficult and often not straightforward to measure the RI of biological materials with high precision [6, 7]. As a matter of fact, there is no experimental measurement on the RI for individual virus particles. How heterogeneous these particles are in their RI values is not known.

Currently, label-free detection or biosensing of animal viruses is under fast development [8–15]. Among different biosensor designs, an increasing group of biosensors works by detecting the local change in the RI due to the mere presence of a single or a few virion particles [16]. Optical biosensors of this type include the use of optical cavity resonance [17–19], optical interferometry [20–25], or surface plasmon resonance [26–28]. In order to quantitate the size and concentration of viruses from these RI-based biosensors, the precise RI for the virions of interest is required [9, 18, 21, 24]. For example, the maximum spectral shift caused by the adsorption of a single virion is a function of the viral RI in whispering-gallery mode (WGM) virus sensors [18]. In a sensor based on surface plasmon resonance, the RI of the virions is needed to calculate the density of the virions bound on an antibody-coated sensing surface [24]. In sensors based on optical interferometry, the RI of a virion is also required for the size measurement of individual virions [9, 21].

Although a diverse set of viruses has been the subjects of interest for detection using these optical methods, none of these studies has ever measured the RI for the virus of interest. In lieu of experimental measurements, the RI value of the virus is often assumed to be certain values. These values varied from 1.41 to 1.57 (Table 1), although the rationale behind these assumptions has not been validated. An experimental method is, therefore, much needed to directly measure the RI of animal virions. Because virus samples are often heterogeneous and it is difficult to obtain them in high purity [29–31], this method should be implemented at single-particle level so that the potential heterogeneity across different particles can be assessed.

Table 1. Summary of RI values assumed in various viral sensing studies.

Virus of interest	RI values assumed	Reference
M13 bacteriophage	1.57	[17]
Influenza A virus	1.5	[18]
HIV-1	1.5	[21]
Herpes simplex virus type 1	1.41	[24]
Influenza A virus	1.48	[28]

In this work, we present a new method based on optical tweezers that allows experimental measurement of the RI of a spherical nanoparticle with high precision, and apply it to individual human immunodeficiency viruses type-1 (HIV-1) virions. When a single nanoparticle is optically trapped, the trap stiffness can be related to the size and RI of the trapped particle by solving the second order derivative of the electric potential energy relative to space [32]. Because both the particle size and the trap stiffness can be measured simultaneously for each trapped particle [33, 34], the RI of that particle can thus be uniquely determined. These measurements yielded an RI of 1.42 for individual HIV-1 virions. Despite the fact that these virions display size heterogeneity as large as 16%, the coefficient of variance (CV) for the RI only amounts to 1.4%. This result suggests that it is the material instead of the size of these virions that dominates the value of their RI. To the best of our

knowledge, this is the first experimental measurement of the RI for individual animal viruses and the assessment of RI heterogeneity across individual particles. This method can be readily applied to other dielectric nanoparticles, and yield the label-free parameter that can be used for particle detection and potential sorting in fluid.

2. Material and methods

2.1 Production of HIV-1 virions

HIV-1 virions were generated and assayed as described recently [35]. Briefly, 293T cells were transfected with 1.0 μg pNL4-3R⁻ E⁻ plasmid, 0.1 μg pEnv (NL4-3 envelope expression plasmid) and 0.3 μg pEGFP-Vpr using Mirus LT-1 transfection reagents in 2 ml culture volume in a 35 mm dish. The medium was changed 6 h post-transfection, and virions were harvested at 24 h post transfection. Infectious virion concentrations were measured using the TZM-bl indicator cell line, and the physical concentrations of virion particles were determined using a p24 enzyme-linked immunosorbent assay (ELISA) as previously described [35].

2.2 Preparation of unilamellar liposomes encapsulating sucrose

The unilamellar liposomes encapsulating 2.0 M sucrose solution were prepared by the established lipid hydration and extrusion method [36]. Briefly, a round-bottom glass vial was rinsed three times with chloroform. ~500 μl egg PC dissolved in chloroform (25mg/ml, cat#840051C, Avanti Polar Lipids) was added to the tube. The chloroform was evaporated to form a thin lipid film by blowing Argon down the side of the tube while rotating the vial. After the lipid film was dry, the glass vial was sealed with aluminum foil and transferred to a vacuum desiccator. The foil was poked with holes using 30G needles, and then vacuum was withdrawn for 2 hours to further dry the lipid film. At the end of desiccation, we added 1 ml 2.0 M sucrose solution to the vial to hydrate the lipid film. The lipids were resuspended in solution by vortex several times until all lipids films were in suspension, and then further incubated at 4°C overnight. On the second morning, the hydrated lipid mixture was first heated in 65°C water bath for 5 min, and then extruded using a Lipofast extruder (Avestin) pre-heated at 65°C. The lipids were extruded by passing through 1 micron pore size membranes, followed by 100 nm pore size membranes, each for 10 times. The resulting liposomes were collected from the original empty side of the extruder and stored 4°C in an Eppendorf tube. For optical trapping experiments, the liposome stocks were diluted in PBS and used for trapping. The stability of these liposomes encapsulating 2.0 M sucrose in PBS was assessed by measuring the size of these liposomes in PBS as a function of time using photo correlation spectroscopy (Malvern Instruments). The diameters of the liposomes measured from samples immediately after dilution in PBS and incubated at 20°C for various time until 8 hours after dilution were all identical with error, displaying no dependence on time.

2.3 Optical trapping experiments

A home-made optical tweezers instrument using a tapered amplifier diode laser (SYS-420-830-1000, Sacher LaserTechnik LLC) was used for optical trapping, back-focal-plane (BFP) interferometry and simultaneous two-photon fluorescence (TPF) measurement of HIV-1 virions [37]. The laser has a wavelength of 830 nm in the air. Briefly, the trapping laser was focused to a diffraction limited spot using a $\times 60$ water-immersion microscope objective (Nikon) with a numerical aperture of 1.2. For polystyrene (Spherotech) and silica (Bangs Laboratory) particles, they were diluted in milli-Q water, sonicated in a benchtop cup sonicator (Misonix S-4000 Ultrasonic processor) at a power setting of 100 for 60 seconds, and injected into a microfluidic chamber for optical trapping. Live virus stock was freshly thawed from -80°C freezer and diluted in complete media, consisted of DMEM

supplemented with 10% fetal bovine serum (Hyclone), to a concentration of 4×10^7 virions ml^{-1} and injected directly into a microfluidic chamber for optical trapping without sonication. HIV-1 virions are identified by the TPF signal emitted from the EGFP fluorophores internally tagged to the viral core, excited by the trapping beam, as described previously [33]. A laser power of 130.8 mW at the focus was used throughout for optical trapping and simultaneous TPF excitation. The laser power was monitored using a position-sensitive detector and kept within 1% variation throughout all experiments. Brownian motion of the trapped particles was recorded using BFP interferometry [38] at 62.5 kHz for 10 s [39]. To measure the particle diameter, a closed-loop nanopositioning stage (3D200, Mad City Labs) was used to sinusoidally oscillate the microfluidic chamber along x- or y-axis at a defined frequency and amplitude [34]. Control experiments showed that oscillation did not induce any change in the thermal background. The particle radius and trap stiffness were calculated as described previously [33]. All the trapping experiments were conducted at a constant temperature of 20.0 ± 0.2 °C unless otherwise noted.

2.4 Viscosity and bulk measurement of RI

The viscosities of the complete media and that of PBS were measured using an Ubbelohde Semi-Micro viscometer (Cannon) at the same temperature as the trapping experiments were performed, following manufacturer's instructions. The RI of the complete media was measured using an Abbe refractometer under ambient light. The RI of the complete media at 830 nm was then calculated to be 1.3307 ± 0.0002 at 830 nm by assuming the same dispersion function as that of water. The RI of 2.0 M sucrose solution was measured using an Abbe refractometer under ambient light.

3. Results and discussion

3.1 Single particles of different materials display distinct values of trap stiffness

To demonstrate the quantitative dependence of optical trap stiffness on the RI of the trapped nanoparticle, we have chosen to work with nanospheres made of polystyrene or silica, whose size are close to those of animal viruses but with known RI. These spheres were diluted in milli-Q water, followed by sonication to reduce the potential aggregates (Materials and Methods), and then injected into a microfluidic chamber for optical trapping (Fig. 1(a)). Although these nanospheres are not visible to the eye under bright field illumination, we could clearly detect the trapping of these particles from changes in laser deflection at the objective's back focal plane. As shown in Fig. 1(b), the arrival of a polystyrene nanoparticle at the optical trap immediately produced a laser deflection signal that was distinct from the background. For each trapped particle, the time course of this laser deflection signal can be converted to a power spectrum in the frequency domain (Fig. 1(c)), which reflects the damped Brownian motion of the trapped particle in a harmonic potential formed by the optical trap [34, 40]. A distance standard can be added into this power spectrum by oscillating the microfluidic chamber at a defined frequency with a known amplitude (the spike at 10 Hz in Fig. 1(c)), which allows calculation of the particle diffusion coefficient and the trap stiffness with high accuracy [33, 34].

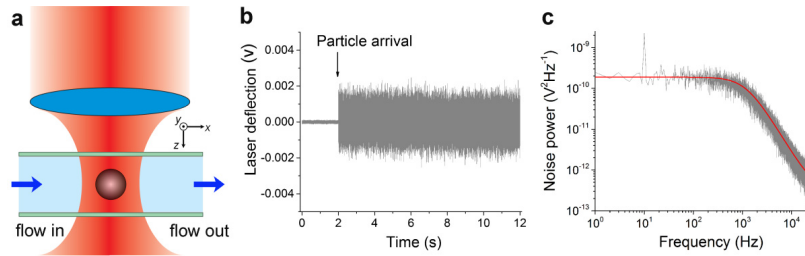


Fig. 1. BFP interferometry to determine nanoparticle radius and trap stiffness. (a) nanoparticles were delivered into a microfluidic chamber and trapped by the IR laser focused at the center of the chamber. The xyz dimensions are shown as indicated, with y perpendicular to the figure plane. (b) The laser deflection signal measured in real time using BFP interferometry for a polystyrene sphere. The signal shown was along y -axis. (c) The power spectrum of the trapped polystyrene sphere from (b) when the chamber was oscillated at 10 Hz with amplitude of 208 nm along y -axis of the sample plane. The red curve is fitting of the thermal noise background to aliased Lorentzian with $D^{\text{volt}} = 2.68 \times 10^{-3} \text{ V}^2/\text{s}$ and $f_c = 1198 \text{ Hz}$ [33].

Because these particles are spheres or very close to spheres, we can thus determine their radii using the Stokes-Einstein equation. As shown in Fig. 2(a), the polystyrene spheres display a mean radius of $97 \pm 15 \text{ nm}$ ($N = 66$), which is in close agreement with the radius of these particles that we determined previously using transmission electron microscopy [33]. The uncertainties reported throughout this work represent standard deviations unless noted otherwise. The distribution of trap stiffness for these polystyrene particles is shown in Fig. 2(b), with a mean of $16.1 \pm 3.4 \text{ fN/nm}$. Figures 2(c) and 2(d) show the distributions of particle size and trap stiffness for silica spheres. Although these silica spheres have a mean radius of $81 \pm 15 \text{ nm}$ ($N = 101$) that is comparable to that of polystyrene spheres, the mean trap stiffness is only $6.7 \pm 1.8 \text{ fN/nm}$, which is more than twofold lower than that of polystyrene spheres. This difference in trap stiffness cannot be simply explained by their differences in particle size using the Rayleigh scattering approximation, nor other factors such as resonances in high RI particles (relative RI >1.5) [41], or forces induced by WGM [42]. Rather, it suggests that the difference in the RI of the material that makes up these particles contribute substantially to these differences in the trap stiffness. Silica spheres may have a lower RI than polystyrene spheres; as a consequence, the lower dielectric contrast between silica spheres and the aqueous medium results in a weaker trapping force and thus a lower trap stiffness.

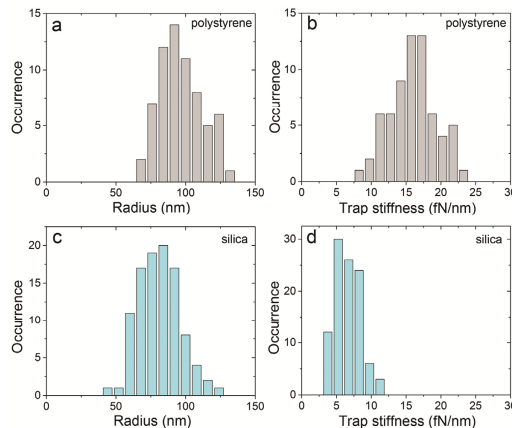


Fig. 2. Particle radius and trap stiffness measured for polystyrene and silica spheres using BFP interferometry. (a) and (b), distributions of particle radius and trap stiffness for polystyrene spheres ($N = 66$). (c) and (d), distributions of particle radius and trap stiffness for silica spheres ($N = 101$).

3.2 Method to extract RI from size and trap stiffness for a single nanoparticle

For particles that are much smaller than the wavelength of the light, the so-called Rayleigh scatterer, quantitative theories exist in relating the trap stiffness with the size and RI of the particle [43, 44]. To meet the criteria for a Rayleigh scatterer, the figure of merit $4\pi n_0 R/\lambda$ needs to be much smaller than unity [45], where n_0 is the RI of the medium, R is the radius of the particle, and λ is the wavelength of the light. This figure of merit calculated for the above polystyrene or silica particles is greater than unity. As a consequence, the closed-form expressions that exist in literature for Rayleigh particles [43] or micro-sized particles [46] do not apply. To extract RI from the observed differences in trap stiffness, we have thus derived a closed-form expression that relates optical trap stiffness with the size and the RI for particles in this range of interest. This analytical solution is based on a potential energy model developed by Tlusty *et al.* for a particle in a single-beam gradient optical trap [32]. This model computes the electric potential energy of a particle in the optical trap by integrating the light intensity over the particle volume, and can be applied to particles bigger than Rayleigh scatterer, as we demonstrate below.

For a non-resonant dielectric particle with a small susceptibility, the electric potential energy of the particle in an electric field can be calculated by integrating the unperturbed electric energy density over the volume of the particle [32]:

$$W = -\alpha \int I(\rho, z) dV \quad (1)$$

where I is the energy density of the electric field, and $\alpha = n_p^2/n_0^2 - 1$ accounts for the relative difference between the RI of the particle n_p and that of the surrounding medium n_0 . For the ease of calculation, we will use a cylindrical coordinate system to describe I throughout, and ρ and z define the transverse and axial coordinates in this system (Fig. 3).

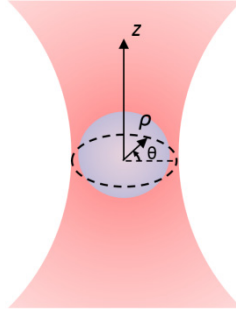


Fig. 3. Schematic of the cylindrical coordinate system for computation of the trap stiffness as a function of particle radius. The origin of the system is located at the focal point of the beam. The z -axis points along the beam axis, consistent with the representation in Fig. 1(a); and ρ points along the transverse dimension, which is perpendicular to the beam axis z . The electric field of the beam before focusing is polarized in the direction where the azimuth angle $\theta = 0$.

Because all particles studied in this work are close to spheres, we have thus conducted this volume integral over a sphere for all these different particles. Once the potential energy W is calculated, the trap stiffness κ for the particle can then be derived as the second spatial derivative of the potential energy. In the transverse dimension that is perpendicular to the trapping beam axis, this can be expressed as:

$$\kappa = \frac{\partial^2 W}{\partial \rho^2} \quad (2)$$

where ρ is the radial distance in a cylindrical coordinate system.

For the above calculation, one needs to know the spatial distribution of $I(\rho, z)$ in order to perform the volume integration. For an optical trap that is formed by a Gaussian beam focused through a high-numerical aperture (NA) objective, the full derivation of the photon energy density at the laser focus has been published [47]. Based on this derivation, the spatial distribution of $I(\rho, z)$ can be numerically calculated, as shown in Fig. 4(a)-4(c) for each vectorial component of the photon electric field together with their sum (Fig. 4(d)) at the focal plane after passing through an objective with an NA of 1.2. This calculation has high precision, but it becomes increasingly sophisticated to numerically evaluate its volume integration and derivative based on Eq. (1) and Eq. (2). Because the particles of our interest are smaller than 160 nm in their radii, we surmise that the non-Gaussian components in $I(\rho, z)$ (E_y and E_z as shown in Fig. 4(b)-4(c)) will have only a minor contribution to the overall trap stiffness. To test this, we have numerically calculated the trap stiffness induced by the total field intensity (the blue curve in Fig. 4(e)), and compared it to that induced by the Gaussian component alone (E_x^2 , the red curve in Fig. 4(e)). This comparison shows that these two curves are largely overlapping with each other for particles with a small radius. As a matter of fact, the differences in the resulting trap stiffness are less than 2% for particles that are smaller than 160 nm in radius (Fig. 4(f)). This difference is only significant for relatively large particles as compared to the beam waist, and it vanishes for smaller particles.

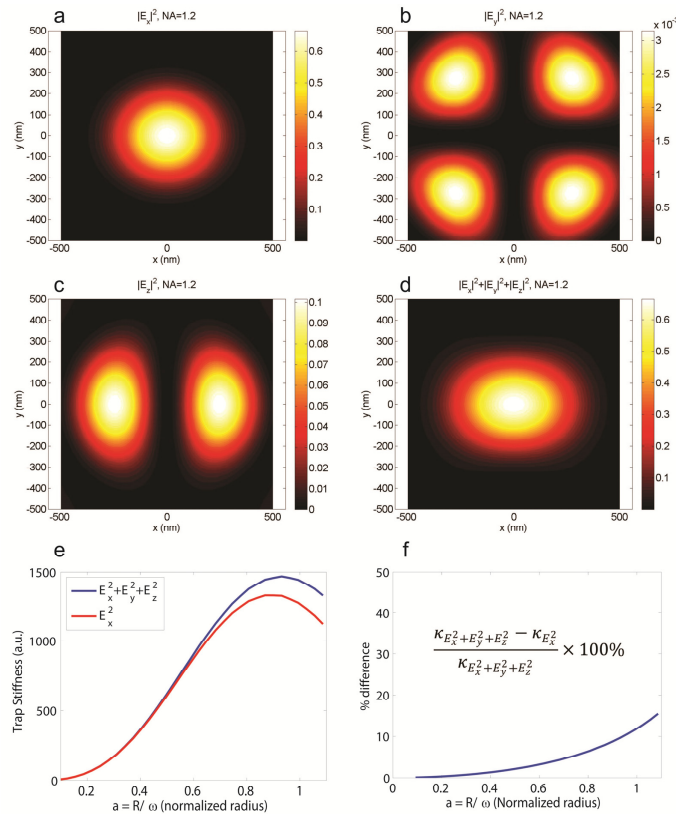


Fig. 4. Validation of the paraxial approximation for the optical forces exerted by a highly focused TEM₀₀ laser beam on a nanoparticle. (a – c) The x, y, and z components, and (d) the total intensities of the electric field of the photons at the focal plane for a fully vectorial, diffraction limited focal spot formed by an objective with numerical aperture (NA) = 1.2. (e) The transverse trap stiffness induced by the total field intensity ($E_x^2 + E_y^2 + E_z^2$) as compared to that induced by E_x^2 only. The value of ω , which is the radius of the beam waist, is set to 322 nm as calculated for the diffraction limited, vectorial field at the beam focus. (f) Percentage difference in the trap stiffness as shown in e.

These results indicate that for particles of our interest, we can safely apply the so-called paraxial approximation of a Gaussian beam, i.e., only considering the Gaussian component of the beam, without introducing significant systematic errors. In a cylindrical coordinate system (Fig. 3), the time-averaged energy density distribution for a Gaussian beam profile is described as follows [48]:

$$I(\rho, z) = I_0 \left(\frac{\omega_0^2}{\omega(z)^2} \right) \exp\left(-\frac{2\rho^2}{\omega(z)^2} \right) \quad (3)$$

where $\omega(z) = \omega_0 \sqrt{1 + \left(\frac{\lambda z}{\pi \omega_0^2} \right)^2}$ is the radius at which the laser beam energy density I drops to I/e^2 of the axial value, $\omega_0 = \omega(0)$ is the radius of the beam waist, and $I_0 = I(0, 0)$ is the energy density at the center of the beam waist.

Using Eq. (3) for energy density, one can numerically integrate Eq. (1) and solve for trap stiffness using Eq. (2), and further evaluate this model by fitting experimental data with simulations based on this model. However, no analytical solution to Eqs. (1) and Eqs. (2) is available with this authentic Gaussian beam profile as $I(\rho, z)$. To overcome this limitation, we have used a three-dimensional (3D) Gaussian profile in a cylindrical coordinate system to represent $I(\rho, z)$ as shown in the following equation:

$$I(\rho, z) = I_0 \exp\left(-\frac{2\rho^2}{\omega_0^2} - \frac{2z^2}{\omega_0^2 \varepsilon^2} \right) \quad (4)$$

where I_0 is the energy density at the center of the beam waist, ω_0 and $\omega_0 \varepsilon$ are the radii of the beam waist in the transverse and axial directions, respectively, with ε being the beam eccentricity.

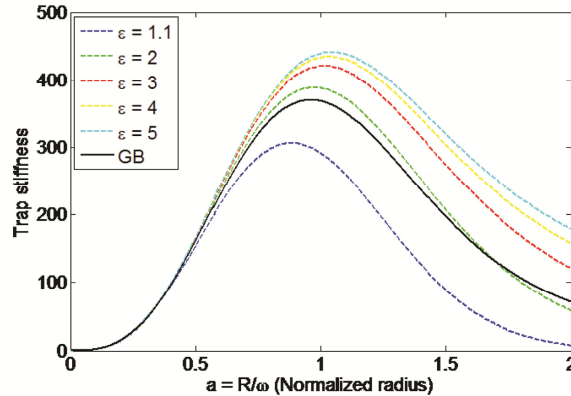


Fig. 5. Validation of the 3D Gaussian profile in lieu of an authentic Gaussian beam to represent the field energy density. The trap stiffness (a.u.) as a function of particle radius normalized to the radius of the beam waist is shown above. These simulations were done for polystyrene particles. For authentic Gaussian beam profile, we have numerically calculated trap stiffness as a function of particle radius using Eq. (1), Eq. (2), and Eq. (3), and the result is shown in black solid curve. For 3D Gaussian profile to represent the field energy density, we have calculated trap stiffness as a function of particle radius using Eq. (1), Eq. (2), and Eq. (4). We have tested different values of the eccentricity ε varying from 1.1 to 5, and the results are shown in dashed lines as indicated. The same beam parameters of I_0 and ω_0 were used for all these simulations.

As shown in Fig. 5, this 3D Gaussian profile provides a very good approximation for an authentic Gaussian beam in relating trap stiffness with particle size. Among different values

of ε that we have tested, a beam eccentricity value of 2 provides the closest agreement with an authentic Gaussian beam (Green dashed curve in Fig. 5). This approximation is even better for those particles whose radius is smaller than that of the beam waist, such as HIV-1 virions. Most importantly, the use of Eq. (4) for $I(\rho, z)$ allows us to derive an analytical solution for the trap stiffness based on the RI and radius of a particle, as shown below in Eq. (5),

$$\kappa = \alpha I_0 \omega_0 \frac{2\pi}{\xi^3} \left[\sqrt{2\pi} \left((\xi a)^2 + \frac{1}{4} \right) e^{-2a^2} \operatorname{erfi}(\sqrt{2}a\xi) - \xi a e^{-2a^2/\varepsilon^2} \right] \quad (5)$$

Where κ corresponds to the transverse trap stiffness on a particle with radius R and a RI of n_p , $\alpha = n_p^2/n_0^2 - 1$, with n_0 being the RI of the medium, $a = R/\omega_0$ is the particle radius normalized by the beam waist, and $\xi = \sqrt{1 - \varepsilon^{-2}}$.

Equation (5) differs from Eq. (8) derived by Tlustý et al. [32]. However, we noticed that Eq. (2) in Tlustý et al. is incorrectly represented. The correct equation to describe the field energy density for a 3D Gaussian profile should be Eq. (4), as we show in current study. The availability of an analytical expression to relate trap stiffness with the RI and radius of a nanoparticle is important for several reasons. First, to help understand the implications of Eq. (5), we rewrite Eq. (5) as follows,

$$\kappa = \alpha I_0 \omega_0 \frac{2\pi}{\xi^3} F(R, \omega_0, \varepsilon) \quad (5a)$$

where $F(R, \omega_0, \varepsilon)$ stands for the portion inside the square bracket in Eq. (5), which is a function of particle radius R , beam parameters ω_0 and ε . As a result, under a constant set of trapping conditions where beam parameters including I_0 , ω_0 , and ε are fixed, the trap stiffness will only be influenced by α , the dielectric contrast between the particle and the medium, and the radius of the particle R . Particles of the same radius will display trap stiffness that is directly proportional to α . Second, the availability of a closed-form expression allows us to use nonlinear least squares fitting to directly evaluate how well this function describes trap stiffness for a nanoparticle. Because we have measured the particle size and trap stiffness for individual polystyrene and silica spheres under the same laser power (Fig. 2), using the known values of RI for polystyrene [49] and silica [50] respectively, we can fit the data from individual nanoparticles to Eq. (5) and derive the beam parameters I_0 and ω_0 . As shown in Fig. 6, the fitting using Eq. (5) yields the red solid lines, with a reduced χ^2 value of 1.02 and 1.03 for polystyrene and silica spheres, respectively, indicating that Eq. (5) provides a very good description for both data. Moreover, this fitting also yields two sets of beam parameters I_0 and ω_0 that are in close agreement with each other (Table 2), which further supports the validity of Eq. (5), and implies that we work in an unperturbed regime, i.e., particles have small dielectric contrast with the surrounding medium and induce negligible perturbation to the electric field.

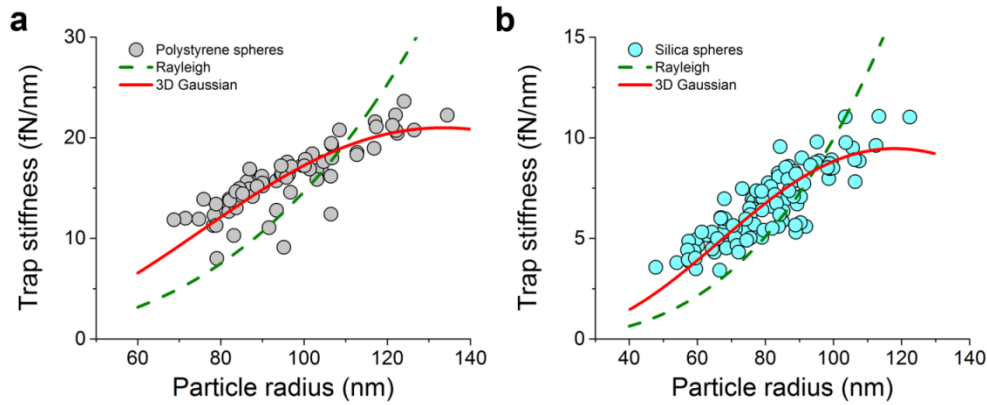


Fig. 6. Quantitative dependence of trap stiffness on particle radius. (a) The dependence of trap stiffness on particle radius for polystyrene spheres ($N = 66$). The experimental data are shown in grey spheres. (b) The dependence of trap stiffness on particle radius for silica spheres ($N = 101$). The experimental data are shown in light cyan spheres. For both panels, the red solid curves represent the results from nonlinear least squares fitting of the experimental data using Eq. (5), with a beam eccentricity $\epsilon = 2$. The green dashed lines represent the results from nonlinear least squares fitting of the experimental data using Rayleigh scatterer (the cubic dependence).

Table 2. Summary of parameters in the nonlinear least square fitting of trap stiffness as a function of radius for individual polystyrene and silica spheres, respectively.

Type of particle	Particle RI used (n_p)*	Beam eccentricity used (ϵ)	Energy density (I_0) from fitting (kJ/m^3)	Radius of beam waist (ω_0) from fitting (nm)	Reduced χ^2 from fitting
polystyrene	1.577	2	0.115 ± 0.002	137 ± 4	1.02
silica	1.453	2	0.123 ± 0.004	121 ± 7	1.03

*The published RI of polystyrene at 833 nm is 1.577 [49]. The published RI of fused silica at 830 nm is 1.453 [50].

For comparison, we also tested fitting of our experimental data using the Rayleigh approximations, assuming these spheres are Rayleigh scatterers, which would predict a cubic dependence between the trap stiffness and the particle size. The best results from these fittings are plotted as the green dashed lines in Fig. 6, with a reduced χ^2 value of 1.533 and 1.580 for polystyrene and silica, respectively, indicating clearly that the Rayleigh model does not describe these data. These results support our conclusion that these particles are not Rayleigh scatterers. Instead, the potential energy model based on Eq. (5) is required to adequately describe the trapping of these particles. It is worth noting that a non-cubic dependence of trap stiffness on particle size was also reported by Bendix and Oddershede for optical trapping of sucrose-loaded liposomes, whose sizes ranged from 20 to 100 nm in radius [36].

Although the results above were obtained by using beam eccentricity value of 2, we emphasize that the choice of this eccentricity for the 3D Gaussian profile has negligible effects on this fitting. As shown in Fig. 7, we have fitted the experimental data for polystyrene beads using 3D Gaussian approximations with values of eccentricity ranging from 2 to 5. Good fittings were obtained in all cases. The corresponding fitting parameters, the energy density at the focus, I_0 , the radius of the beam waist, ω_0 , as well as the reduced χ^2 goodness of fitting, are listed in Table 3 for different beam eccentricities. Less than 5% variations are observed in the resulting parameters. This result is expected because the eccentricity only changes the 3D Gaussian profile in the axial dimension, and has minimal impact on the trap stiffness in the transverse dimension.

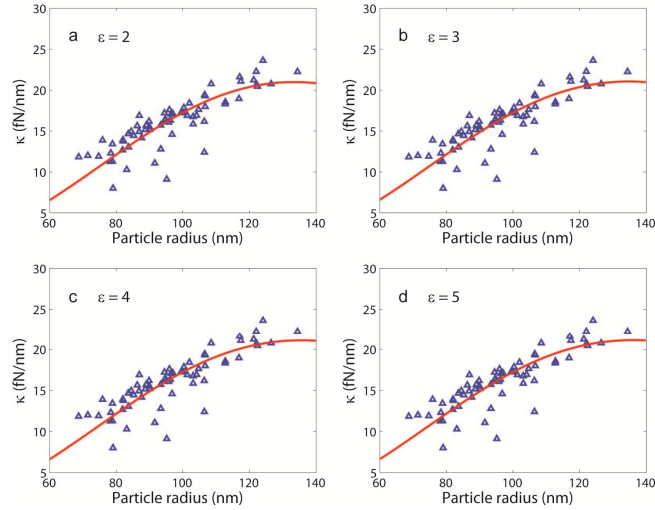


Fig. 7. The value of 3D Gaussian beam eccentricity has negligible effect on the fitting of the trap stiffness. The experimentally measured trap stiffness as a function of particle radius (blue triangles) for polystyrene spheres was fitted using a 3D Gaussian profile with different values of beam eccentricity ϵ . The resulting fits are shown in red solid curves for (a) $\epsilon = 2$; (b) $\epsilon = 3$; (c) $\epsilon = 4$; and (d) $\epsilon = 5$, respectively.

Table 3. Summary of fitted beam parameters and the goodness of fits for polystyrene spheres using 3D Gaussian approximation with different beam eccentricities.

Beam eccentricity (ϵ)	Fitting parameters obtained using polystyrene beads		
	Energy density I_0 (kJ/m ³)	Beam waist radius ω_0 (nm)	Reduced χ^2
2	0.115 ± 0.002	137 ± 4	1.0217
3	0.110 ± 0.002	133 ± 4	1.0212
4	0.108 ± 0.002	131 ± 4	1.0209
5	0.107 ± 0.002	131 ± 4	1.0208

3.3 Estimating the impact of scattering force on the modeling of the trap stiffness

In the Eq. (5) that we derived above for trap stiffness, the scattering force is not considered. As shown in Fig. 6 above, the good agreement between experimental data and fits using Eq. (5) indicates that the impact of scattering force on trap stiffness is perhaps negligible. Is this reasonable? In reality, both the gradient force and the scattering force act on a nanoparticle upon optical trapping. Although the latter vanishes much faster than the former for a sub-wavelength particle, a careful modeling of optical trapping should quantify the impact of scattering force. Scattering force pushes the trapped particle along the beam axis to a position where the scattering force has the same magnitude but opposite sign as the gradient force acting on the same particle. Compared to the beam focus, this displacement of the particle away from the focus will slightly change the electric field experienced by the trapped particle, and especially the beam radius at corresponding z -positions (Fig. 3). To quantify the impact of this displacement on trap stiffness, we assume the scattering force pushes the trapped particle along the beam axis by certain distance P_z away from the focal point, and derived an analytical solution for the transverse trap stiffness κ located at a position $(Pz, 0, 0)$ (refer to the cylindrical coordinates defined in Fig. 3) using Eq. (1), Eq. (2) and Eq. (4) as follows,

$$\kappa = \alpha I_0 \omega_0 \left\{ \begin{aligned} & \frac{4\pi P_z}{9} \left[e^{-(P_z+a)^2/2} - e^{-(P_z-a)^2/2} \right] + \frac{4\pi a}{3} \left[e^{-(P_z-a)^2/2} + e^{-(P_z+a)^2/2} \right] + \\ & \frac{2\sqrt{6}\pi^{\frac{3}{2}}}{9} \left(1 + 3a^2 + \frac{P_z^2}{3} \right) e^{-\frac{2P_z^2}{3}} e^{-\frac{a^2}{2}} \left[\operatorname{erfi}\left(\frac{\sqrt{6}P_z}{6} - \frac{\sqrt{6}a}{2}\right) - \operatorname{erfi}\left(\frac{\sqrt{6}P_z}{6} + \frac{\sqrt{6}a}{2}\right) \right] \end{aligned} \right\} \quad (6)$$

where all the parameters are the same as those defined previously. Figure 8 shows the resulting transverse trap stiffness as a function of the normalized particle radius calculated at different axial position P_z . It is clear that the transverse trap stiffness is insensitive to the axial position of the particle within 50 nm of the axial displacement from the focal point.

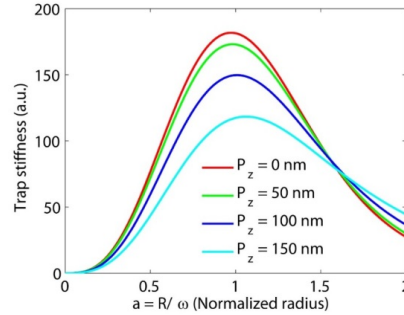


Fig. 8. The impact of scattering force on the modeling of the transverse trap stiffness. Transverse trap stiffness as a function of the particle radius R normalized by the radius of the beam waist ω was analytically calculated using Eq. (6) at different axial displacement values. The displacement of the trapped particle P_z is chosen to be 0 (red), 50 (green), 100 (blue) and 150 (cyan) nm away from the Origin.

The actual displacement of a trapped particle from the focal point is a complex function of the size and material of the trapped particle. For a particle that can be approximated as an electric dipole, this displacement can be estimated using an analytical solution [43]. Using this dipole approximation, a particle with size and RI identical to those of an HIV virion will reside only 6 nm downstream from the focal point along the beam axis. Although single HIV-1 virions are not true Rayleigh scatterers, this estimation suggests that the displacement of an HIV-1 virion from the beam focus is likely to be small. Therefore, we can safely neglect the impact of scattering force on our modeling of the transverse trap stiffness based on the results shown in Fig. 8. In other words, we do not expect the scattering-induced axial displacement of an HIV virion to significantly influence the modeling of the gradient force.

3.4 Measure the RI for individual HIV-1 virions

The results from Fig. 6 suggest a method to measure the RI for spherical dielectric nanoparticles using particles of known RI as a reference. This method will involve the following steps: (a) optically trap the nanoparticles of interest, determine individual particle size and trap stiffness; (b) under the same laser settings, optically trap reference nanoparticles of known RI, from nonlinear least square fitting for these reference particles to determine the two laser beam parameters, the focal-point energy density I_0 and the radius of the beam waist ω_0 ; (c) using Eq. (5) to calculate the RI for each single particle based on the measured particle size, trap stiffness and information on I_0 and ω_0 . The advantage of this closed-form expression is that one can calculate RI for each single particle. This calculation performed over many particles can yield statistical uncertainties on the RI, which allows us to further assess the potential heterogeneity of these particles in the values of their RI.

To measure the RI for individual HIV-1 virions, we freshly diluted frozen stocks of HIV-1 virions in the complete media and delivered them to the microfluidic chamber. Sonication

was not performed in order to preserve the infectivity of these virions. Each HIV-1 virion was identified by their two-photon fluorescence (TPF) from associated enhanced green fluorescent proteins (EGFP). For each individual HIV-1 virion trapped, we measured the particle radius together with the trap stiffness. As noted previously, the distribution of particle radius (Fig. 9(a)) displayed a slight non-Gaussian tail that corresponds to either the natural aggregation of virions [33] or virions with multiple cores [51]. To avoid the potential complication of these large virions on RI measurement, we have chosen to analyze only those particles whose sizes fall within the range of $\mu \pm 2\sigma$ for further analysis, with μ and σ being the mean and standard deviation of the radius for single HIV-1 virions determined by the Gaussian fitting in red curve. As a result, 8 particles were excluded from a total of 97 particles for these HIV-1 virions. These virions display a radius of 74 ± 12 nm, consistent with authentic single HIV-1 virions [51]. Figure 9(b) shows the distribution of corresponding trap stiffness for these virions, with an average stiffness of 3.5 ± 1.0 fN/nm, which is close to half of that for silica spheres. We then used the beam parameters derived from fitting of polystyrene particles (Table 2) to calculate the RI for each HIV-1 virion. Figure 9(c) shows the distribution of RI for these single HIV-1 virions. Most virions display an RI close to 1.42, except one single particle with a distinct value of 1.55. This particle has a diameter of 97 nm, which is smaller than typical HIV-1 virions and thus may be a particle of other nature in the culture medium. Excluding this outlier, the RI for the rest 88 virions has a mean value of 1.42 ± 0.02 , with a median of 1.42. We have calculated the RI for these virions using the beam parameters derived from fitting of polystyrene spheres but with different values of eccentricity. The results are all identical within error (1.42 ± 0.02). We also calculated the RI for these virions using the beam parameters derived from fitting of silica spheres, which resulted in a decrease of RI by only 0.4% in both mean and median, suggesting the robustness of this method. Moreover, the CV of the RI for these HIV-1 virions is 1.4%, despite the fact that these virions carry 16% CV in their radius. This 1.4% CV is threefold smaller than the CV expected from error propagation based on ensemble variations in the particle size and trap stiffness, and suggests that the RI determined using our method has a high precision. This high precision may stem from the fact that we simultaneously measure the particle size and trap stiffness for each individual particle, which takes particle size heterogeneity into explicit account. This precision also allows us to conclude that it is the material that makes up these virions that dominates the value of RI, even though these particles have size variations as large as 16%.

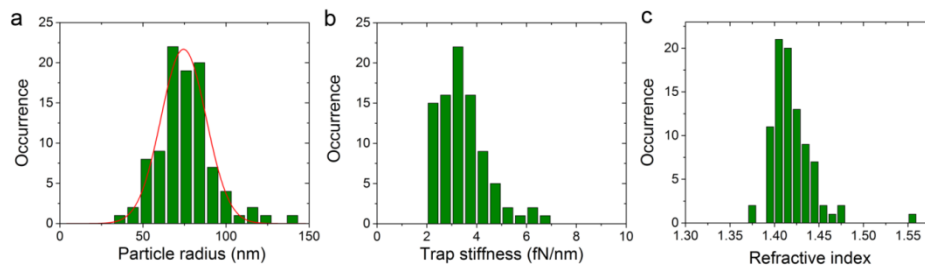


Fig. 9. Measurement of HIV-1 to determine the RI of single virions. (a) Distribution of particle radius measured for HIV-1 virions using BFP interferometry ($N = 97$). The red solid curve is a fit to Gaussian distribution. (b) Distribution of trap stiffness measured for single HIV-1 virions ($N = 89$). (c) Distribution of RI calculated for single HIV-1 virions using Eq. (5) ($N = 89$).

The derivation of Eq. (5) has several important assumptions. First, it requires the particle to be spherical and less than 160 nm in radius (Fig. 4(f)); second, the field energy density should not be significantly perturbed by the presence of the particle; and third, it assumes that the particle has a singular value of RI that describes its interaction with photon electric field. Although the first and second assumptions can be well justified for individual HIV-1 particles as they are largely spherical [51, 52] and has low dielectric contrast with the surrounding

medium, it has not been tested whether a single value of RI for the entire particle is adequate to describe the resulting trap stiffness as a function of the particle size. This concern is valid given the apparent heterogeneities in material makeup and distributions within a single HIV-1 virion. It is known that HIV-1 viral particles are made of several different major materials (proteins, nucleic acids and lipids) and individual mature virions carry conical-shaped viral cores inside each particle [51]. These aspects are quite different from individual polystyrene or silica particles. However, the results above in Fig. 9 indicate that a single mean value of RI for HIV-1, with low CV, quantitatively describes the trap stiffness in relation to particle size. This result suggests that the trap stiffness may not be sensitive to the aforementioned heterogeneities within a single spherical particle, and whether this holds for other biological nanoparticles remains to be tested in the future.

3.5 Validate the RI measurement of HIV-1 virions using liposomes

The above data for HIV-1 virions yielded a mean RI value of 1.42 at 830 nm that is substantially lower than that of polystyrene or silica spheres. Although this may be a reflection of the content of HIV-1 virions that is different from polystyrene or silica, this result also raises the question about our reference standard. Whether our method will work well for particles with RI outside the range of reference particles is unknown. To address this issue, we have prepared unilamellar liposomes encapsulating 2 M sucrose solution as our test particles. Previously, unilamellar liposomes loaded with sucrose solution has been used to demonstrate optical trapping of nanoscale particles with small inducible dipole moment [36]. Bendix and Oddershede have demonstrated that even under 1 W of laser power [36] these sucrose-loaded particles remain as spherical particles with negligible deformations. We trapped these particles, measured their radii and the trap stiffness. As shown in Fig. 10(a), the radius distribution for these particles show a predominant peak around 70 nm ($N = 142$). From this distribution, it is also clear that there are aggregates of liposomes that have radii greater than 100 nm. To focus on single liposome particles for RI calculation, we have fitted this radius distribution to a single Gaussian, which resulted in a mean radius of 68 ± 15 nm. We then selected the particles whose sizes fall within the range of $\mu \pm 2\sigma$ for further calculation of RI. As shown in Fig. 10(b), the average trap stiffness from these liposomes encapsulating 2 M sucrose is 2.3 ± 0.8 fN/nm ($N = 124$), which is slightly lower than that of HIV-1 virions. Based on these data, the mean RI for these liposomes derived from Eq. (5) is 1.41 ± 0.02 ($N = 124$) at 830 nm, with a median of 1.41, as shown in Fig. 10(c), which compares very well to the RI of 1.430 for 2.0 M sucrose under ambient light that we measured using a refractometer (Materials and Methods). The slightly lower value at 830 nm can be explained by RI dispersion as a function of wavelength, in which the RI of a liquid decreases monotonically as the wavelength of the light increases [53, 54]. For eight different liquids including water, it has been measured that the RI decrease varies from 0.0078 to 0.0432 in changing from 500 nm to 830 nm, with an average decrease of 0.018 [55]. Thus, the 0.02 RI differences that we have observed for sucrose solution from ambient light refractometer and optical trapping measurement appear reasonable. In conclusion, our measurement of RI for single HIV-1 virions (1.42 at 830 nm) is thus trustworthy, because our reference samples have RI values ranging from 1.41 to 1.577 at 830 nm.

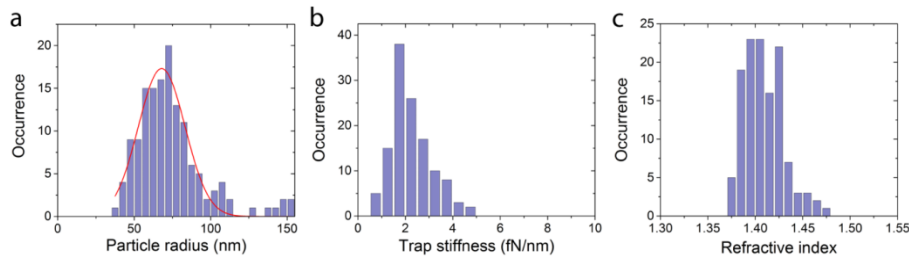


Fig. 10. Measurement of unilamellar liposomes encapsulating 2.0 M sucrose. (a) Distribution of particle radius measured for liposomes using BFP interferometry ($N = 142$). The red solid curve is a fit to Gaussian distribution. (b) Distribution of trap stiffness measured for single liposome particles ($N = 124$). (c) Distribution of RI calculated for single liposomes using Eq. (5) ($N = 124$).

3.6 The high precision of the RI measurement

Despite the heterogeneity of these particles in their size, the measured RI only has a CV of 1.4%, true for both HIV-1 virions and liposomes encapsulating 2.0M sucrose solution. This small variation in their RI suggests that it is the material of the particle that dominates the value of RI. This precision may result from the simultaneous measurement of the particle size and trap stiffness for each single particle. In doing so, the size variation of nanoparticles is considered explicitly so that the uncertainty in the particle size from a group of heterogeneous particles is not propagated through the calculation at the ensemble level [56–58]. As a matter of fact, a previous measurement of RI for bacteriophages reported an uncertainty of 6%-10% [56]. A highly accurate RI will be critical in working with ultrasensitive optical biosensing setups, which typically have $10^{-6} - 10^{-8}$ refractive index unit sensitivity [14]. The uncertainty in the particle RI, if any, can be further amplified during the operation of optical sensors as a result of a low dielectric contrast between the analyte and the surrounding medium. For example, in a WGM virus sensor, a 6% uncertainty in the virus RI will result in a 101% uncertainty in the maximum spectral shift predicted for the adsorption of a virus according to the error propagation analysis [18]. In contrast, a 1.4% uncertainty in the virus RI only results in a 24% uncertainty in the maximum spectral shift. This comparison highlights the need for a highly accurate RI in biosensing applications, which is achievable with our current technique.

3.7 Additional issues for the use of current method

As indicated by our results in Fig. 4(f), our method applies to particles less than 160 nm in radius, for which the paraxial approximation can be applied without causing significant errors. It remains to be determined whether in reality there is a size limit below which our method may fail. A very important issue in current technique to measure the RI with high precision is the temperature at the optical trap. Because the viscosity of water changes sensitively with temperature, one wants to make sure the heating effect from laser trap is either negligible or taken into account. We use 830 nm laser for optical trapping, as we have shown previously the heating effect by this laser is negligible in aqueous solution [33, 37]. However, this may not be true for other wavelength such as 1064 nm, where water absorbs fivefold stronger than 830 nm. In that case, care should be taken to ensure that the temperature and viscosity used match those at the optical trap. HIV-1 virion preparation contains microvesicles [30, 31, 59]. In our current measurement, we use EGFP tagged internally to virion particles to distinguish between authentic HIV-1 virions and microvesicles [60]. These EGFP molecules make up less than 0.1% of the mass for the entire virion [61], thus we expect the presence of these proteins will only have minimal influence on the RI of the virus. On the other hand, because we can now measure the RI for individual virion particles with high precision, we may use this RI as a potential label-free parameter to distinguish between authentic unlabeled HIV-1 virions and microvesicles that are devoid of

viral contents, and then determine whether the presence of these EGFP tag molecules inside HIV-1 virions may have any measurable effects on the RI. Lastly, the current method assumes an unperturbed photon electric field upon trapping of a particle. It might be feasible in the future to develop this method to include trapping conditions where the field is perturbed, provided that a quantitative description for the perturbed field is available.

4. Conclusion

Despite the importance of RI for label-free detection of viruses, no experimental measurement on the RI for any animal virus is available. In this paper, we have derived and tested a closed-form expression that relates optical trap stiffness with the size and the RI of a trapped nanoparticle Eq. (5). Based on this equation, we have developed a method to measure the RI for individual spherical nanoparticles with high precision. Our measurement reveals that HIV virion has an RI of 1.42 ± 0.02 at 830 nm. To the best of our knowledge, this is the first experimental report on the RI of a single animal virus. This value is substantially lower than the RI typically assumed for many other viruses (Table 1), but close to that of a concentrated sucrose solution. Among others, we postulate that significant empty space within each particle due to the incompleteness of the Gag shell during virion assembly and budding [62] may contribute to this value of RI. Majority of viruses have a radius in between 15 and 150 nm [63]. As we demonstrate, the analytical expression to relate trap stiffness with particle size and RI in Eq. (5) can be applied to individual dielectric particles whose radii are below 160 nm, and thus ideally suited for biological nanoparticles such as viruses, certain drug delivery particles, or extracellular vesicles. We expect this method to be widely applicable to biological nanoparticles, and may be used as a standard to assess and correct any theoretical estimation. The availability of a precision RI will now allow people to model optical forces on these nanoscale biological particles using numerical methods such as T-matrix approach [64]. As a label-free parameter of materials, the high precision in RI measurement also allows one to assess potential heterogeneity of the particles due to differences in their materials, and potentially distinguish biological nanoparticles of different nature in a label-free manner.

Acknowledgments

This work was supported by NIH Director's New Innovator Award 1DP2OD008693-01 to WC, NSF CAREER Award CHE1149670 to WC and also in part by Research Grant No. 5-FY10-490 to WC from the March of Dimes Foundation. We thank Cheng Lab members for helpful discussions. The following reagents were obtained through the AIDS Research and Reference Reagent Program, Division of AIDS, National Institute of Allergy and Infectious Diseases (NIAID), National Institutes of Health (NIH): pNL4-3 from Dr. Malcolm Martin; pNL4-3.Luc.R-E- from Dr. Nathaniel Landau; pEGFP-Vpr from Warner C. Greene; TZM-bl cells from Dr. John C. Kappes, Dr. Xiaoyun Wu and Tranzyme Inc.